Published in final edited form as:
Nat Phys. 2020 January ; 16(1): 75–82. doi:10.1038/s41567-019-0683-5.

A coherent nanomechanical oscillator driven by single-electron tunnelling

Yutian Wen[1], **N. Ares**[1], **F.J. Schupp**[1], **T. Pei**[1], **G.A.D. Briggs**[1], **E.A. Laird**[2,1,*]

[1]Department of Materials, University of Oxford, Parks Road, Oxford OX1 3PH, United Kingdom

[2]Department of Physics, Lancaster University, Lancaster, LA1 4YB, United Kingdom

Abstract

A single-electron transistor embedded in a nanomechanical resonator represents an extreme limit of electron-phonon coupling. While it allows fast and sensitive electromechanical measurements, it also introduces backaction forces from electron tunnelling that randomly perturb the mechanical state. Despite the stochastic nature of this backaction, it has been predicted to create self-sustaining coherent mechanical oscillations under strong coupling conditions. Here, we verify this prediction using real-time measurements of a vibrating carbon nanotube transistor. This electromechanical oscillator has some similarities with a laser. The single-electron transistor pumped by an electrical bias acts as a gain medium and the resonator acts as a phonon cavity. Although the operating principle is unconventional because it does not involve stimulated emission, we confirm that the output is coherent. We demonstrate other analogues of laser behaviour, including injection locking, classical squeezing through anharmonicity, and frequency narrowing through feedback.

Backaction forces are an inescapable accompaniment to nanomechanical measurements. While their ultimate limit is set by quantum uncertainty[1], in practical devices they may become significant even well before this limit is reached. Among the most sensitive nanomechanical probes is the single-electron transistor (SET), which transduces motion with a precision that can approach the standard quantum limit[2,3]. However, the price is that the force exerted even by individual electrons modifies the mechanical dynamics. This introduces strong electron-phonon coupling[4–6], which has usually been recognised by its incoherent effects such as dissipation, frequency softening, nonlinearity, and cooling[7]. Here, we show that electromechanical backaction can also have a coherent result, by harnessing it to create a self-sustained mechanical oscillation. The resulting device is analogous to a laser, where the optical field is replaced by the mechanical displacement. In contrast to existing

*Electronic address: e.a.laird@lancaster.ac.uk.

Data availability The data that support the plots within this paper and other findings of this study are available from the corresponding authors upon reasonable request.

Author Contributions Y.W. fabricated the device following a recipe devised by T.P., and performed the experiment and analysis with contributions from N.A., F.S. and E.A.L. Y.W. and E.A.L. wrote the manuscript. All authors discussed results and commented on the manuscript.

Competing financial interests The authors declare no competing financial interests.

Europe PMC Funders Author Manuscripts

phonon lasers pumped by optical or mechanical drives[8–10], the oscillator is driven by a constant electrical bias. The device exhibits several laser characteristics, detected via its electrical emission, including phase and amplitude coherence. It serves both as a novel on-chip phonon source and to explore the connection between the physics of backaction and of lasers.

To enter this regime of strong backaction, the SET, serving as a two-level system, must couple strongly to a mechanical resonator serving as a phonon cavity (Fig. 1a). As a high-quality resonator, we use a suspended carbon nanotube[11]. Nanotubes have both low mass and high mechanical compliance, which are favourable for strong electron-phonon interaction[5,6,12–14]. The selected nanotube is a narrow-gap semiconductor, allowing the SET to be defined in the nanotube itself using tunnel barriers at each end and a conducting segment near the middle. The two relevant SET states are the configurations with and without an excess electron. Flexural vibration of the nanotube modulates the electrical potential experienced by the SET, causing the current to vary with displacement; at the same time, each added electron exerts a force that is larger than both quantum and thermal force fluctuations (see Supplementary Information).

The combination of these effects sets up an electromechanical feedback with rich predicted behaviour[15]. If the SET's energy splitting is resonant with the mechanical frequency, electrical excitations should be able to pump the resonator in a direct analogue of the micromaser[16]. More surprisingly, a laser-like instability is predicted even in a non-resonant situation, with complex dynamics that depend on level alignment and damping, and go beyond conventional laser behaviour[17,18]. Previous experiments measuring time-average current through a nanotube have provided strong evidence for a threshold between resonance and oscillation[5,19,20]. However, to test these predictions by fully characterizing the resulting states requires time-resolved displacement measurements[21,22], which have not yet been possible in this regime of strong backaction.

Backaction turns a resonator into an oscillator

To explore these dynamic effects, we implemented an electromechanical circuit for measuring the nanotube's vibrations directly[12] (Fig. 1b). The carbon nanotube is stamped across metallic contact electrodes[23] to give a vibrating segment of length 800 nm, and is measured at a temperature of 25 mK. Voltages applied to five finger gates beneath the nanotube (labelled G1-G5) are used both to tune the electrical potential and to actuate vibrations by injecting an RF tone with drive power P_D. A voltage bias V_{DS} is applied between the contacts to drive a current I. To configure the nanotube as an SET, the gate voltages are set to tune an electron tunnel barrier near each contact. The conductance thus depends strongly on the displacement, which allows sensitive electromechanical readout via the current through the nanotube. The radio-frequency (RF) part of the current is passed through an impedance transformer and then amplified, with the primary amplifier being an ultra-low-noise SQUID[24]. Since this current varies approximately in proportion to the instantaneous displacement, the resulting RF output voltage V_{out} is a sensitive time-resolved record of the mechanical vibrations

To identify signatures of electromechanical feedback, we first measure the DC conductance as a function of bias and DC gate voltage V_G applied to gate G2 (Fig. 2a). Superimposed on the diamond pattern characteristic of single-electron charging are irregular sharp ridges of strongly positive or negative conductance as the nanotube switches between high and low-current states. Such features are associated with the onset of mechanical instability for bias exceeding a critical threshold[5,18].

We detect the mechanical resonance by fixing the bias voltage and measuring the transmission of the drive tone to the RF amplifier input, using a scalar network analyser. When the drive frequency matches the mechanical resonance, the resulting motion relative to the gate electrodes changes the chemical potential of the SET, modulating the current at the drive frequency. This current, entering the impedance transformer, excites an RF output voltage V_{out}. The RF output signal voltage is therefore proportional to the nanotubes displacement, apart from the contributions of nonlinear SET transconductance and of RF electrical leakage[12]. For most gate voltage settings, these contributions are small. The mechanical resonance therefore appears as a sharp peak in the electrical transmission from the drive to the output (Fig. 2b). The resonance frequency fluctuates quasiperiodically with gate voltage, which is a further indication of electromechanical coupling and arises because the effective spring constant is softened close to a Coulomb charge transition[5,6]. From the peak width, the mechanical quality factor is $Q_M \approx 1.8 \times 10^4$, with some gate voltage dependence because of electromechanical damping.

Mechanical oscillations, as distinct from a mechanical resonance, become evident when the output power spectrum is measured without driving using a spectrum analyser (Fig. 2c). This undriven emission, plotted as a power spectral density S referenced to the amplifier input, shows a peak whose frequency approximately follows the resonance of Fig. 2b. The peak is only present for some gate voltage settings, and is brightest close to the transport ridges of Fig. 2a. Furthermore, this peak strengthens with increasing bias (see Supplementary Information). For some gate voltage settings on the right of the graph, the peak switches between two or more frequencies, suggestive of dynamical bifurcation. All these observations imply that the observed emission is a result of self-excited mechanical oscillations driven by the DC bias across the device.

Mechanical coherence

With fast electromechanical readout, the coherence of this mechanical oscillator can be directly confirmed by measuring the output signal in real time. To do this, the signal is mixed with a local oscillator in a heterodyne circuit[26,27] to generate records of the in-phase and quadrature voltages $V_I(t)$ and $V_Q(t)$ as a function of time t. The output record (Fig. 3a) shows clear sinusoidal oscillations. The onset of mechanical coherence is seen when the in-phase and quadrature time traces are represented as two-dimensional histograms for gate voltage settings above and below the oscillation threshold. Below threshold, the histogram is peaked near the origin, consistent with a band-limited but quasi-thermal source such as a randomly kicked resonator (Fig. 3b). However, above threshold the histogram has a ring shape, showing amplitude coherence characteristic of a laser-like oscillator (Fig. 3c). The

ring diameter corresponds to an approximate phonon number $\bar{n}_p \sim 10^5$, i.e. an oscillation amplitude of ~ 1 nm, although there is a large uncertainty because of unknown device parameters (see Supplementary Information).

The clearest comparison to an ideal classically coherent source comes from a histogram of total output power, which is proportional to the number of phonons in the mode (Fig. 3d). Below threshold, the histogram follows the exponential distribution of completely incoherent quasi-thermal emission[26]. Above threshold, the histogram shifts to a distribution where the most probable state has a non-zero output power, as expected for a coherent source. It is approximately fitted by a Gaussian distribution, characteristic of a coherent oscillator in the limit of large phonon number $\bar{n}_p$. However, the distribution is slightly skewed, while its width, which for an ideal coherent state would be $\sim \sqrt{\bar{n}_p}$, is much larger than expected. Both the excess width and the skew indicate additional noise in the oscillator, presumably due to complex feedback between motion and electron tunnelling. The faint spot at the centre of Fig. 3c indicates bistability[18,28], where the nanotube is either below threshold or has switched to a different frequency outside the measurement bandwidth. The weight of the spot shows that for this gate setting the device spends approximately 0.5 % of its time in such a state[26].

While amplitude coherence is shown by the histogram, phase coherence is determined by plotting the autocorrelation of the demodulated signal $g^{(1)}(\tau)$ as a function of time interval τ (Fig. 3e). For these settings, the data are well fitted by an decaying sinusoid, reflecting the slow phase drift of the free-running oscillator. The envelope decay gives a phase coherence time $\tau_{coh} = 99\ \mu s$, i.e. a coherence linewidth of $\delta f_{coh} = 1/\pi\tau_{coh} = 3$ kHz, approximately three times narrower than the mean resonance linewidth f_M/Q_M (See Supplementary Data). The emission spectrum shows no dependence of linewidth on temperature up to 700 mK (data not shown). Coherence is further confirmed by plotting the second-order correlation function $g^{(2)}(\tau)$, which shows chaotic quasi-thermal behaviour below threshold but nearly coherent behaviour above threshold[25] (Fig. 3f).

As the gate voltage is swept, the device switches between oscillating and non-oscillating states, and both the power and coherence time change (Fig. 4). By simultaneously measuring the RF and DC signals, the consequences for DC transport can be seen. Figure 4a shows current as a function of gate voltage over several periods of Coulomb blockade, while Fig. 4b shows the coherence time and emission power P_{total} over the same range. The oscillator switches on and off approximately once per Coulomb period. Both the coherence time and the emitted power vary irregularly, but as expected most switches between oscillating and non-oscillating conditions coincide with abrupt current changes.

At least three theoretical mechanisms allow an electrical current to create the positive feedback force that drives coherent oscillations. When two energy levels, for example in a double quantum dot, are misaligned by a multiple of the phonon energy[29], positive feedback occurs through conventional stimulated emission[26]. However, such a condition should occur at precise gate voltage settings, whereas Fig. 2c shows emission across a wide range of gate voltage. Another possible mechanism is electrothermal, in which the thermal mass of the

resonator delays the expansion or contraction due to ohmic heating[30]. While this mechanism may contribute in our device, the sign of the feedback should be proportional to dI/dV_G. However, Fig. 4 shows oscillations occur on both sides of the Coulomb peaks. We therefore attribute the oscillations mainly to a third mechanism; the combination the SET's capacitance with delayed electron tunnelling. When the tunnel barriers are such that the usual dependence of the SET's charge on displacement is inverted, this creates the required positive feedback force[17,18] (see Supplementary Information).

Injection locking and anharmonic effects

While the phase coherence time extracted from the autocorrelation characterizes the long-term oscillator stability, it is limited by slowly varying extrinsic effects such as charge noise or adsorbed atoms[13]. To evaluate sensing schemes that rely on detecting mechanical frequency shifts, it important to identify the oscillator's intrinsic linewidth if this slow variation could be eliminated, which may be much narrower. To measure the intrinsic linewidth, we employ two techniques from laser spectroscopy to stabilise the oscillator frequency.

First, we demonstrate that the oscillator can be locked to a stable but weak seed tone applied to the gate[32,33]. This phenomenon of injection locking, previously demonstrated for trapped ions[34] and driven mechanical resonators[35], arises because feedback amplifies small forces close to the operation frequency. In this measurement, the emission is monitored while the seed tone is applied at a nearby frequency f_D (Fig. 5). As seen in Fig. 5a, b, for a range of f_D settings near the free-running oscillator's frequency and with sufficient drive power P_D, the broad emission line collapses onto the injection frequency. The locking events are accompanied by steps in the DC current (Fig. 5c, d).

The frequency range Δf_D over which the oscillator is locked extends over many linewidths. Figure 5e shows the locking range as a function of injected power, confirming that a stronger injection tone has greater frequency pull. The data are well fitted by a power law of the form $f_D = AP_D^{\alpha}$, where A and α are fit parameters. However, whereas the theory of conventional oscillators[31] predicts an exponent $\alpha = 0.5$, the data show a smaller exponent $\alpha \sim 0.3$.

A second unexpected feature is a pair of weak spectral satellites, marked by arrows in Fig 5a-b. To investigate these further, Fig. 5f shows the emission spectrum as a function of injection power across the transition to locking. Surprisingly, the satellite offset frequency Δf_{side} depends on injection power, with a dependence that is approximately $\Delta f_{side} \propto P_D^{0.3}$ (Fig. 5g).

Both the anomalous locking range and the sidebands can be explained by the oscillator's anharmonicity, which modifies the conventional theory of injection locking in harmonic oscillators. As recently demonstrated in a high-quality nanowire, similar satellites can appear when the anharmonic frequency shift is much larger than the linewidth[36]. They arise because the fluctuations of the displacement about its stationary driven value experience an effective restoring spring constant which is modified by the anharmonicity and therefore different from the resonator's bare spring constant[37]. The effective spring constant may

differ between fluctuations in magnitude and phase, leading to classically squeezed fluctuations; the degree of squeezing can be inferred from the relative intensities of the satellites.

In this respect the nanotube oscillator behaves very differently from an anharmonic (Duffing) resonator. In an anharmonic resonator, the satellites are asymmetric[36], with the ratio of their intensities never greater than $\tanh^2 \frac{1}{4} \ln 3 \approx 0.27$; however, in Fig. 5f the intensity ratio is close to unity. The reason is illustrated in Fig. 5h and explained further in the Supplementary Information. In an anharmonic driven resonator, a perturbed state orbits the stationary point in the rotating frame, which when transformed to the lab frame gives sidebands in the displacement spectrum. An elliptical orbit contains a higher spectral weighting at the frequency corresponding to its sense of rotation, and therefore transforms to asymmetric sidebands. In the anharmonic driven oscillator, the orbits can become very elongated, because the self-feedback stabilises magnitude but not phase. Such an orbit contains nearly equal components in both rotation senses, and therefore generates symmetric sidebands. This is an indication that the injection-locked oscillator generates a classically squeezed state, in the sense that the displacement variance is much larger in the phase quadrature than in the amplitude quadrature.

By solving the equations of motion including a Duffing restoring force (proportional to displacement cubed) in the limit of strong driving and weak damping (see Supplementary Information), both f_D and Δf_{side} are found to be proportional to $P_D^{1/3}$. This is in good agreement with the data (Fig. 5e, g). A numerical solution not assuming strong drive gives slightly better fit for Δf_{side} (Fig. 5g).

Stabilisation through feedback

While injection locking clearly stabilises the oscillator's state, it also contaminates the output spectrum with the high-frequency seed tone. An improved way to measure the oscillator's intrinsic linewidth is to use feedback to cancel out slow frequency wander. To implement this (Fig. 6), the oscillator is incorporated into a phase-locked loop using an error signal voltage fed to gate G1 (see Methods). Figure 6a shows dramatic frequency narrowing when the feedback is turned on. With optimised control parameters, the stabilised linewidth is $\delta f < 2$ Hz (Fig. 6b), which is limited by the spectral frequency spacing and implies over 10^8 coherent oscillations at the operating frequency of 230 MHz. This represents an upper limit on the intrinsic linewidth, and shows it is limited by slowly varying environmental perturbations, such as voltage noise, substrate switchers, and changing surface contamination, rather than by intrinsic damping or by high-frequency noise, which the feedback does not cancel. It is the linewidth that the free-running oscillator would achieve if these slow perturbations could be eliminated by better fabrication or filtering. Similar to the Schawlow-Townes limit on a laser's linewidth[38], the ultimate linewidth for an oscillator without stimulated emission is[39] $\delta f_{ult} = f_M / 4\bar{n}_p Q_M \sim 0.3\,\text{Hz}$.

As expected, the feedback circuit succeeds in concentrating nearly the entire output into a narrow spectral line, provided that the oscillator's free-running frequency is close to the

target frequency (Fig. 6c, d) The stabilisation range is set by the maximum feedback voltage. However, feedback stabilises part of the emission even when this condition is not met, as seen by a weak spectral peak persisting beyond the expected voltage range (Fig. 6d). This indicates that the oscillator occasionally deviates by several linewidths from its central frequency. Feedback makes these excursions visible by temporarily capturing them.

Conclusion

The dynamical instability explored here is an extreme consequence of invasive displacement measurement. For many kinds of nanomechanical sensing, it is a nuisance, because it means that the large bias necessary for precise measurement also strongly perturbs the displacement. However, when the aim is to detect a small frequency shift (e.g. for mass spectrometry[40] or some force-detected magnetic resonance schemes[41]), introducing feedback directly into the sensing element can be beneficial. Clearly, the external frequency stabilization schemes described in the previous section are not directly useful for sensing because they render the oscillator insensitive both to the undesirable drift and to the desirable signal (unless these can be separated spectrally). However, even without applying external stabilization, the oscillation linewidth is narrower than the resonance linewidth, just as a laser's emission is narrower than its cavity linewidth[17], making small shifts easier to detect.

A complement to this instability induced by positive feedback (negative damping) is nanomechanical cooling induced by negative feedback (positive damping). This should occur when the electromechanical contribution to the damping rate becomes positive, and may allow cooling below the refrigerator temperature, possibly down to few phonons. Unfortunately, in our experiment the measurement sensitivity, which ws limited by amplifier noise and by inefficient conversion from displacement to signal voltage, was not sufficient to resolve Brownian motion (see Supplementary Information). Further cooling may have occurred at some gate voltage settings, but was not resolved here.

The similarities between SET nanomechanics and laser physics are intriguing[16,17]. Like a laser, this device combines a pumped two-level system with a boson cavity, and shows phase and amplitude coherence as well as self-amplification. It differs from a conventional laser by not requiring degeneracy between the SET and the resonator, since there is no stimulated emission. A desirable feature of a true phonon laser is that it should emit directionally into a propagating sound wave[42], which this experiment (like previous phonon laser realisations[8–10]) does not test. However, to the extent that the key laser characteristic is output coherence[43], this experiment does indeed realise a phonon laser. It resembles unconventional lasers such as atom lasers that have coherent output statistics without stimulated emission[44].

Further development from this device could replace the SET with a coherent two-level system such as a double quantum dot[45], a superconducting SET[16], or an electron spin[46,47]. This would allow a phonon laser driven by conventional stimulated emission. Ultimately, superpositions might be transferred between the two-level system and the oscillator, allowing dynamic backaction to be studied in the fully quantum limit.

Europe PMC Funders Author Manuscripts

Methods

IQ tomography

To generate the time traces in Fig. 3a, the amplified emission is mixed with a local oscillator running at a nominal frequency offset by $\Delta f = 15$ kHz below the mechanical frequency. The local oscillator and the IQ mixer are implemented in a Zurich Instruments UHFLI lock-in amplifier. The mixer's two intermediate-frequency outputs, corresponding to the two quadratures of the signal and oscillating at frequency Δf, are low-pass filtered with a 100 kHz cutoff to generate the time traces of Fig. 3a. Histograms and autocorrelation traces are built up from 1 s of data at each voltage setting. For the data of Fig. 4, in which the oscillator frequency changes with gate voltage, the local oscillator is adjusted at each voltage setting to maintain approximately constant frequency offset Δf.

The histograms resulting from these time traces (Fig. 3d) were fitted as follows[26], using the fact that $V^2(t)$ is proportional to the number of phonons. Below threshold, the histogram was fitted assuming a quasi-thermal distribution

$$P\left(V^2\right) \propto e^{-V^2/V_{\mathrm{T}}^2}, \tag{1}$$

with V_{T} as a free parameter. Above threshold, the fit is

$$P\left(V^2\right) \propto e^{-\left(V^2 - V_0^2\right)^2/\sigma_V^4} + A_{\mathrm{T}} e^{-V^2/V_{\mathrm{T}}^2} \tag{2}$$

with V_0, σ_V, V_{T} and A_{T} as free parameters, where the two terms represent a Gaussian distribution over phonon numbers and a small quasi-thermal contribution, respectively.

The sharpness of the central spot in Fig. 3c compared with the ring in Fig. 3c and spot in Fig. 3b confirms that these latter features are broadened by intrinsic device noise rather than by detection noise.

Signal autocorrelation

The autocorrelation is defined as

$$g^{(1)}(\tau) \equiv \frac{\left\langle V_{\mathrm{I}}(t) V_{\mathrm{I}}(t+\tau) \right\rangle}{\left\langle V_{\mathrm{I}}^2(t) \right\rangle}, \tag{3}$$

where the expectation value is calculated over a long time trace. In Fig. 3e, this function is fitted with the exponentially decaying oscillation stated in the caption, with τ_{coh} and Δf as fit parameters. While the fit here is good, at other gate voltages the oscillator sometimes jumps between different frequencies during data acquisition. For Fig. 4b, a more general function is therefore used: $g^{(1)}(\tau) = \mu e^{-\tau/\tau_{\mathrm{coh}}} \cos(2\pi\Delta f\tau) + (1-\mu) e^{-\tau/\tau_{\mathrm{filter}}}$. The first term represents the contribution of the oscillator running at its primary frequency, and the second term represents contributions from other frequencies outside the detection bandwidth. The

additional fit parameters are μ, the fraction of time at the primary oscillation frequency, and τ_{filter}, the decay time of the other contributions.

The second-order correlation function[25] is

$$g^{(2)}(\tau) \equiv \frac{\left\langle V^2(t)V^2(t+\tau)\right\rangle}{\left\langle V^2(t)\right\rangle^2}. \quad (4)$$

For a perfectly coherent source, $g^{(2)}(\tau) = 1$ at all τ, whereas Gaussian chaotic emission has $g^{(2)}(\tau) = 1 + e^{-\pi(\tau/\tau_{\text{coh}})2}$. These are the functions plotted in Fig. 3f.

Feedback stabilization

In the phase-locked loop used for Fig. 6, the amplified emission is first mixed with a local oscillator running at the target frequency to generate a quadrature voltage proportional to the phase error. This error signal is digitised at up to 14.06 MHz and used as input for a proportional-integral-derivative (PID) controller[48] to generate a correction voltage. The correction voltage is filtered with a 350 Hz low-pass cutoff and clipped to a range of ±0.8 mV, before being fed back to gate G1 of the device.

Supplementary Material

Refer to Web version on PubMed Central for supplementary material.

Acknowledgements

We acknowledge A. Bachtold, E. M. Gauger, Y. Pashkin, A. Romito and M. Woolley for discussions and T. Orton for technical support. This work was supported by EPSRC (EP/N014995/1, EP/R029229/1), DSTL, Templeton World Charity Foundation, the Royal Academy of Engineering, and the European Research Council (grant agreement 818751).

References

1. Clerk AA, et al. Introduction to quantum noise, measurement, and amplification. Rev Mod Phys. 2010; 82:1155–1208.
2. Schoelkopf RJ, Wahlgren P, Kozhevnikov AA, Delsing P, Prober DE. The Radio-Frequency Single-Electron Transistor (RF-SET): A Fast and Ultrasensitive Electrometer. Science. 1998; 280:1238–1242. [PubMed: 9596572]
3. LaHaye MD, Buu O, Camarota B, Schwab KC. Approaching the Quantum Limit of a Nanomechanical Resonator. Science. 2004; 304:74–77. [PubMed: 15064412]
4. Mozyrsky D, Hastings MB, Martin I. Intermittent polaron dynamics: Born-Oppenheimer approximation out of equilibrium. Phys Rev B. 2006; 73
5. Steele GA, et al. Strong coupling between single-electron tunneling and nanomechanical motion. Science. 2009; 325:1103–1107. [PubMed: 19628816]
6. Lassagne B, Tarakanov Y, Kinaret J, Daniel GS, Bachtold A. Coupling mechanics to charge transport in carbon nanotube mechanical resonators. Science. 2009; 325:1107–1110. [PubMed: 19628818]
7. Naik A, et al. Cooling a nanomechanical resonator with quantum back-action. Nature. 2006; 443:193–196. [PubMed: 16971944]
8. Vahala K, et al. A phonon laser. Nat Phys. 2009; 5:682–686.

9. Grudinin IS, Lee H, Painter O, Vahala KJ. Phonon laser action in a tunable two-level system. Phys Rev Lett. 2010; 104
10. Mahboob I, Nishiguchi K, Fujiwara A, Yamaguchi H. Phonon lasing in an electromechanical resonator. Phys Rev Lett. 2013; 110
11. Sazonova V, et al. A tunable carbon nanotube electromechanical oscillator. Nature. 2004; 431:284–287. [PubMed: 15372026]
12. Wen Y, Ares N, Pei T, Briggs GAD, Laird EA. Measuring carbon nanotube vibrations using a single-electron transistor as a fast linear amplifier. Appl Phys Lett. 2018; 113
13. de Bonis SL, et al. Ultrasensitive Displacement Noise Measurement of Carbon Nanotube Mechanical Resonators. Nano Lett. 2018; 18:5324–5328. [PubMed: 30062893]
14. Khivrich I, Clerk AA, Ilani S. Nanomechanical pumpprobe measurements of insulating electronic states in a carbon nanotube. Nat Nanotechnol. 2019; 14:161–167. [PubMed: 30643270]
15. Armour AD, Blencowe MP, Zhang Y. Classical dynamics of a nanomechanical resonator coupled to a single-electron transistor. Phys Rev B. 2004; 69
16. Rodrigues DA, Imbers J, Armour AD. Quantum dynamics of a resonator driven by a superconducting single-electron transistor: A solid-state analogue of the micromaser. Phys Rev Lett. 2007; 98
17. Bennett SD, Clerk AA. Laser-like instabilities in quantum nano-electromechanical systems. Phys Rev B. 2006; 74
18. Usmani O, Blanter YM, Nazarov YV. Strong feedback and current noise in nanoelectromechanical systems. Phys Rev B. 2007; 75
19. Hüttel AK, Witkamp B, Leijnse M, Wegewijs M, van der Zant HSJ. Pumping of Vibrational Excitations in the Coulomb-Blockade Regime in a Suspended Carbon Nanotube. Phys Rev Lett. 2009; 102
20. Eichler A, Chaste J, Moser J, Bachtold A. Parametric Amplification and Self-Oscillation in a Nanotube Mechanical Resonator. Nano Lett. 2011; 11:2699–2703. [PubMed: 21615135]
21. Tsioutsios I, Tavernarakis A, Osmond J, Verlot P, Bachtold A. Real-Time Measurement of Nanotube Resonator Fluctuations in an Electron Microscope. Nano Lett. 2017; 17:1748–1755. [PubMed: 28186773]
22. Barnard AW, Zhang M, Wiederhecker GS, Lipson M, McEuen PL. Real-time vibrations of a carbon nanotube. Nature. 2019; 566:89–93. [PubMed: 30664747]
23. Wu CC, Liu CH, Zhong Z. One-step direct transfer of pristine single-walled Carbon nanotubes for functional nanoelectronics. Nano Lett. 2010; 10:1032–1036. [PubMed: 20108926]
24. Schupp FJ, et al. Radio-frequency reflectometry of a quantum dot using an ultra-low-noise SQUID amplifier. 2018
25. Fox, M. Quantum Optics: An Introduction. Oxford University Press; 2006.
26. Liu Y-Y, et al. Semiconductor double quantum dot micromaser. Science. 2015; 347:285–287. [PubMed: 25593187]
27. Cassidy MC, et al. Demonstration of an ac Josephson junction laser. Science. 2017; 355:939–942. [PubMed: 28254938]
28. Pistolesi F, Blanter YM, Martin I. Self-consistent theory of molecular switching. Phys Rev B. 2008; 78
29. Fujisawa T, et al. Spontaneous emission spectrum in double quantum dot devices. Science. 1998; 282:932–935. [PubMed: 9794761]
30. Steeneken PG, et al. Piezoresistive heat engine and refrigerator. Nat Phys. 2011; 7:354–359.
31. Adler R. A Study of Locking Phenomena in Oscillators. Proc IRE. 1946; 34:351–357.
32. Stover HL, Steier WH. Locking of Laser Oscillators by Light Injection. Appl Phys Lett. 1966; 8:91.
33. Liu Y-Y, Stehlik J, Gullans MJ, Taylor JM, Petta JR. Injection locking of a semiconductor double-quantum-dot micromaser. Phys Rev A. 2015; 92
34. Knünz S, et al. Injection locking of a trapped-ion phonon laser. Phys Rev Lett. 2010; 105

35. Seitner MJ, Abdi M, Ridolfo A, Hartmann MJ, Weig EM. Parametric Oscillation, Frequency Mixing, and Injection Locking of Strongly Coupled Nanomechanical Resonator Modes. Phys Rev Lett. 2017; 118
36. Huber JS, et al. Detecting squeezing from the fluctuation spectrum of a driven nanomechanical mode. 2019
37. Stambaugh C, Chan HB. Supernarrow spectral peaks near a kinetic phase transition in a driven nonlinear micromechanical oscillator. Phys Rev Lett. 2006; 97
38. Schawlow AL, Townes CH. Infrared and optical masers. Phys Rev. 1958; 112:1940–1949.
39. Wiseman HM. Light amplification without stimulated emission: Beyond the standard quantum limit to the laser linewidth. Phys Rev A. 1999; 60:4083–4093.
40. Chaste J, et al. A nanomechanical mass sensor with yoctogram resolution. Nat Nanotechnol. 2012; 7:301–304. [PubMed: 22466856]
41. Stipe BC, et al. Electron Spin Relaxation Near a Micron-Size Ferromagnet. Phys Rev Lett. 2001; 87
42. Maryam W, Akimov AV, Campion RP, Kent AJ. Dynamics of a vertical cavity quantum cascade phonon laser structure. Nat Commun. 2013; 4:2184. [PubMed: 23884078]
43. Wiseman HM. Defining the (atom) laser. Phys Rev A. 1997; 56:2068.
44. Öttl A, Ritter S, Köhl M, Esslinger T. Correlations and counting statistics of an atom laser. Phys Rev Lett. 2005; 95
45. Brandes T, Lambert N. Steering of a bosonic mode with a double quantum dot. Phys Rev B. 2003; 67
46. Ohm C, Stampfer C, Splettstoesser J, Wegewijs M. Readout of carbon nanotube vibrations based on spinphonon coupling. Appl Phys Lett. 2012; 100
47. Pályi A, Struck PR, Rudner MS, Flensberg K, Burkard G. Spin-Orbit-Induced Strong Coupling of a Single Spin to a Nanomechanical Resonator. Phys Rev Lett. 2012; 108
48. Ogata, K. Modern control engineering. Prentice Hall; 1970.

Europe PMC Funders Author Manuscripts

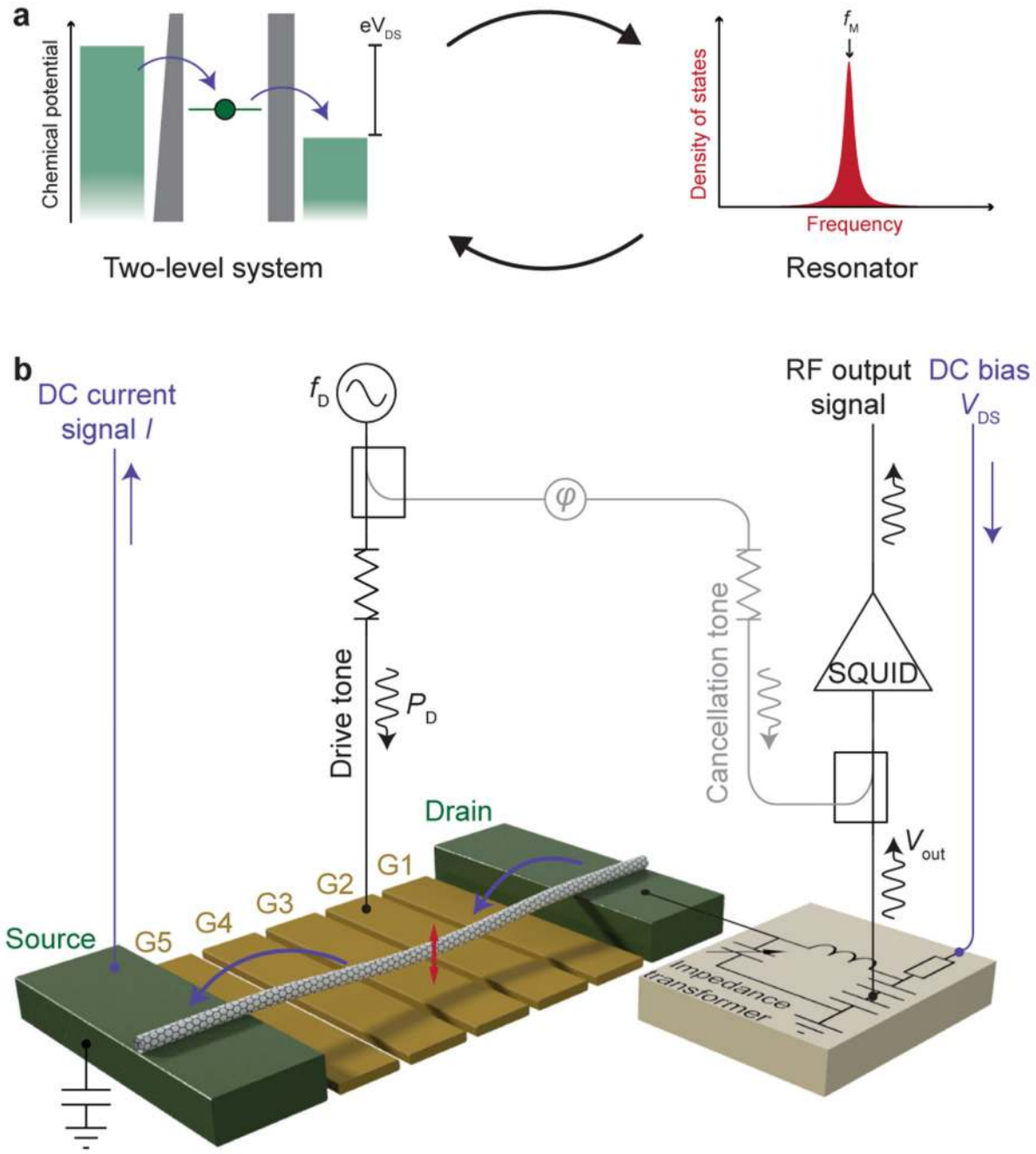

Fig. 1. Strongly coupled single-electron electromechanics.

a, Schematic of a single-electron transistor (SET) coupled to a mechanical resonator. The SET acts as a two-level system, while the resonator is a phonon cavity at mode frequency f_M. Electron tunnelling through the SET leads to a non-equilibrium population distribution which pumps the oscillator. **b**, Device realisation and measurement setup. The vibrating nanotube, configured as an SET, is suspended between contact electrodes (green) and above gate electrodes (yellow). The SET is biased by a drain-source voltage V_{DS}, and the motion is measured via the electrical current, which is monitored both at DC (I, current path indicated

Europe PMC Funders Author Manuscripts

by blue arrows) and via an RF circuit for time-resolved measurements (V_{out}, signal path marked by undulating arrows; see text and Supplementary Information). The resonator can be driven directly by a tone with power P_D at frequency f_D, part of which is routed via a cancellation path to avoid saturating the amplifiers.

Europe PMC Funders Author Manuscripts

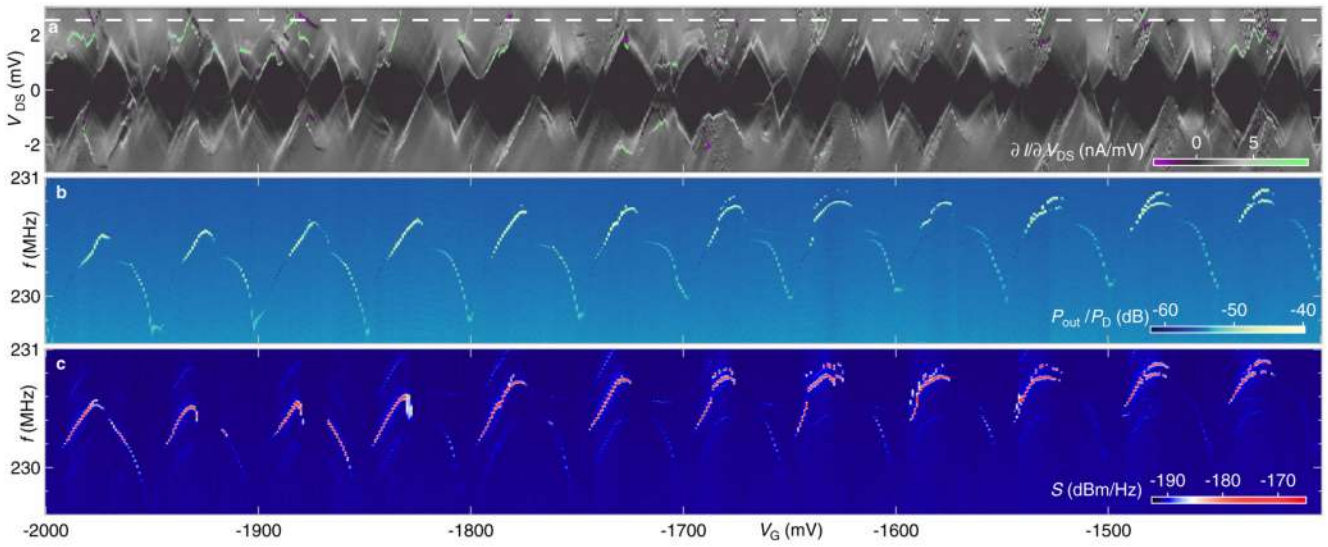

Fig. 2. Mechanical resonance and oscillation

a, Differential conductance of the nanotube as a function of gate voltage V_G and bias V_{DS}, with no driving applied. The diamond pattern is characteristic of Coulomb blockade in an SET, with some irregularity due to electrostatic disorder. Superimposed on the expected diamond pattern are sharp lines of strongly positive or negative differential conductance (green or purple in this colour scale), indicating thresholds for self-oscillation. **b**, Mechanical resonance detected in a transmission measurement. The nanotube is biased with V_{DS} = 2.5 mV (dashed line in **a**) and driven with power P_D = −99 dBm to gate G2. The transmission is plotted as the emitted power P_{out} into the amplifier chain. The mechanical resonance appears as a sharp spectral peak, or occasionally as a faint dip when RF leakage interferes destructively with the mechanical signal. **c**, Emission spectrum density S as a function of frequency f under the same conditions but with no RF drive. A spectral peak is still present, at almost exactly the same frequency as in **b**. This indicates self-driven mechanical oscillations. Faint sidebands to the main signal are artefacts of the SQUID (see Supplementary Information).

Europe PMC Funders Author Manuscripts

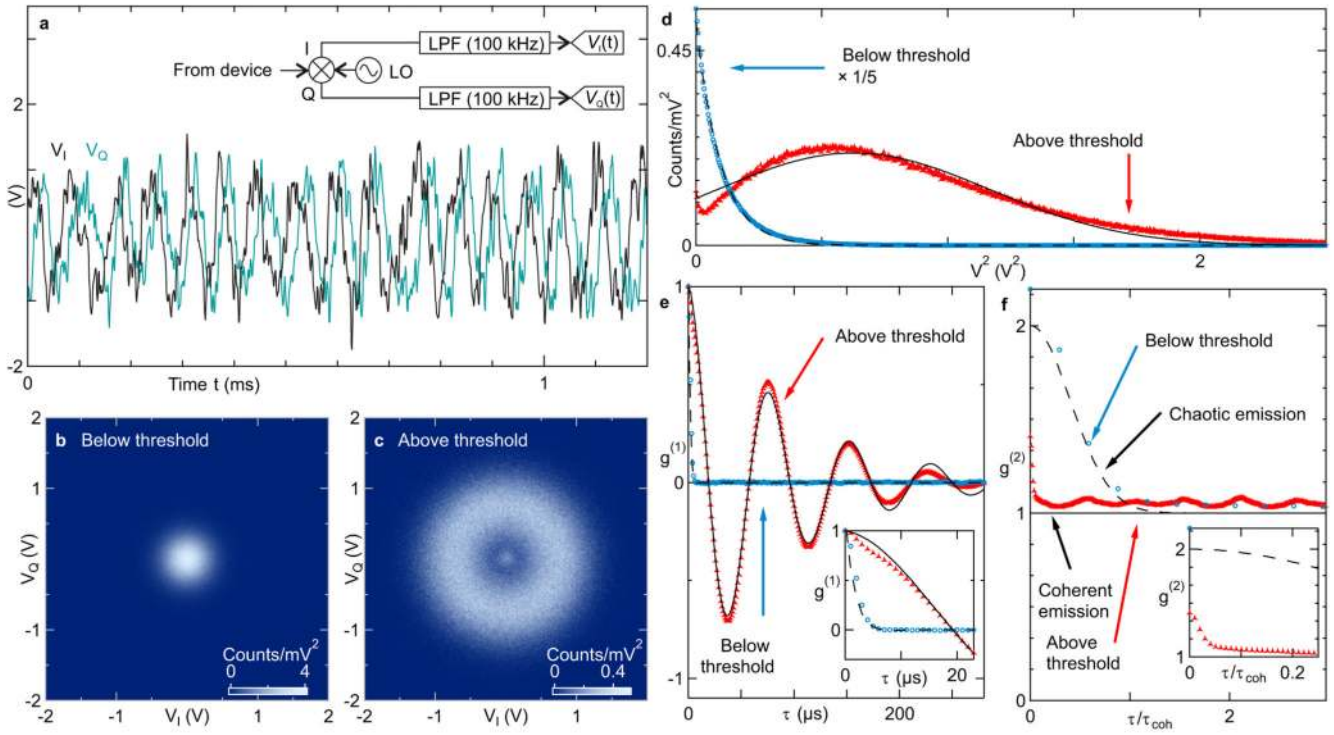

Fig. 3. Coherence of the free-running oscillator.

a, Time traces of in-phase (I) and quadrature (Q) components demodulated from the oscillator output. The heterodyne demodulation circuit is shown in the inset. (LO: local oscillator; LPF: low-pass filter). **b**, Joint histogram of demodulated components with the gate voltage set below the oscillation threshold ($V_G = -1982$ mV). **c**, Histogram when configured above threshold ($V_G = -1568$ mV), showing the characteristic ring of coherent emission. **d**, Symbols: Histograms of total power $V^2(t) = V_I^2(t) + V_Q^2(t)$ below and above threshold, corresponding to the joint histograms in **b, c**. The former is scaled downwards for clarity. Dashed curve: fit to below-threshold data, assuming quasi-thermal source. Solid curve: fit to above-threshold data, assuming a Gaussian distribution of phonon numbers plus a small quasi-thermal fraction. **e**, Symbols: Autocorrelation as a function of time difference τ. Solid curve: Above-threshold fit of the form $g^{(1)}(\tau) = e^{-\tau/\tau_{coh}} \cos(2\pi\Delta f\tau)$, giving coherence time $\tau_{coh} = 99$ μs and heterodyne frequency detuning $\Delta f = 13$ kHz. Dashed curve: Similar fit to below-threshold data with Δf fixed at zero, giving a decay time $\tau_{coh} = 3.3$ μs consistent with the filter bandwidth. **f**, Symbols: Second-order correlation, plotted with respect to the coherence time fitted above. Curves: Parameter-free predictions for Gaussian chaotic emission and for coherent emission[25]. Insets in **e** and **f** are zoom-ins.

Europe PMC Funders Author Manuscripts

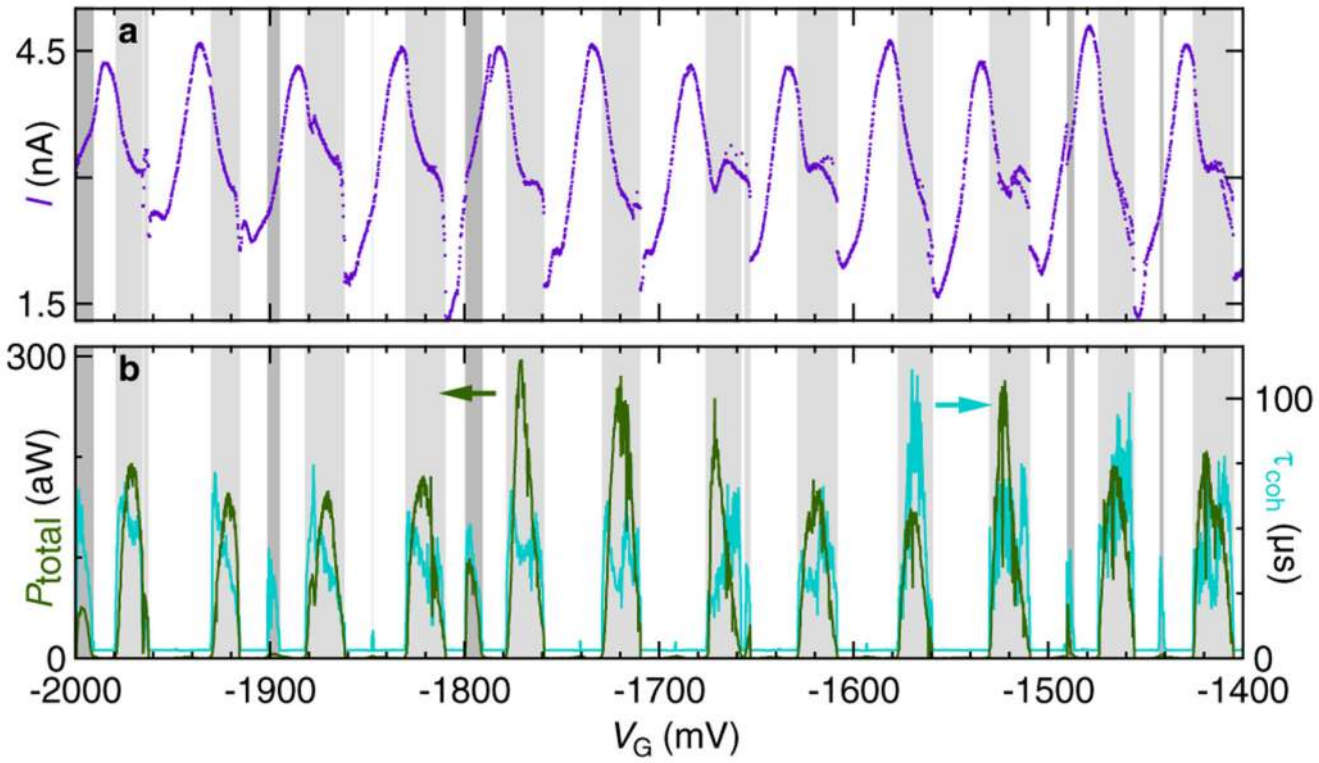

Fig. 4. Tuning the coherence with a gate voltage.

a, The DC current I through the device as a function of gate voltage V_G, with V_{DS} = 2.5 mV and no RF drive. **b**, Simultaneously acquired emission power P_{total} (left axis) and fitted coherence time τ_{coh} (right axis). Shading marks voltage settings with detectable emission.

Europe PMC Funders Author Manuscripts

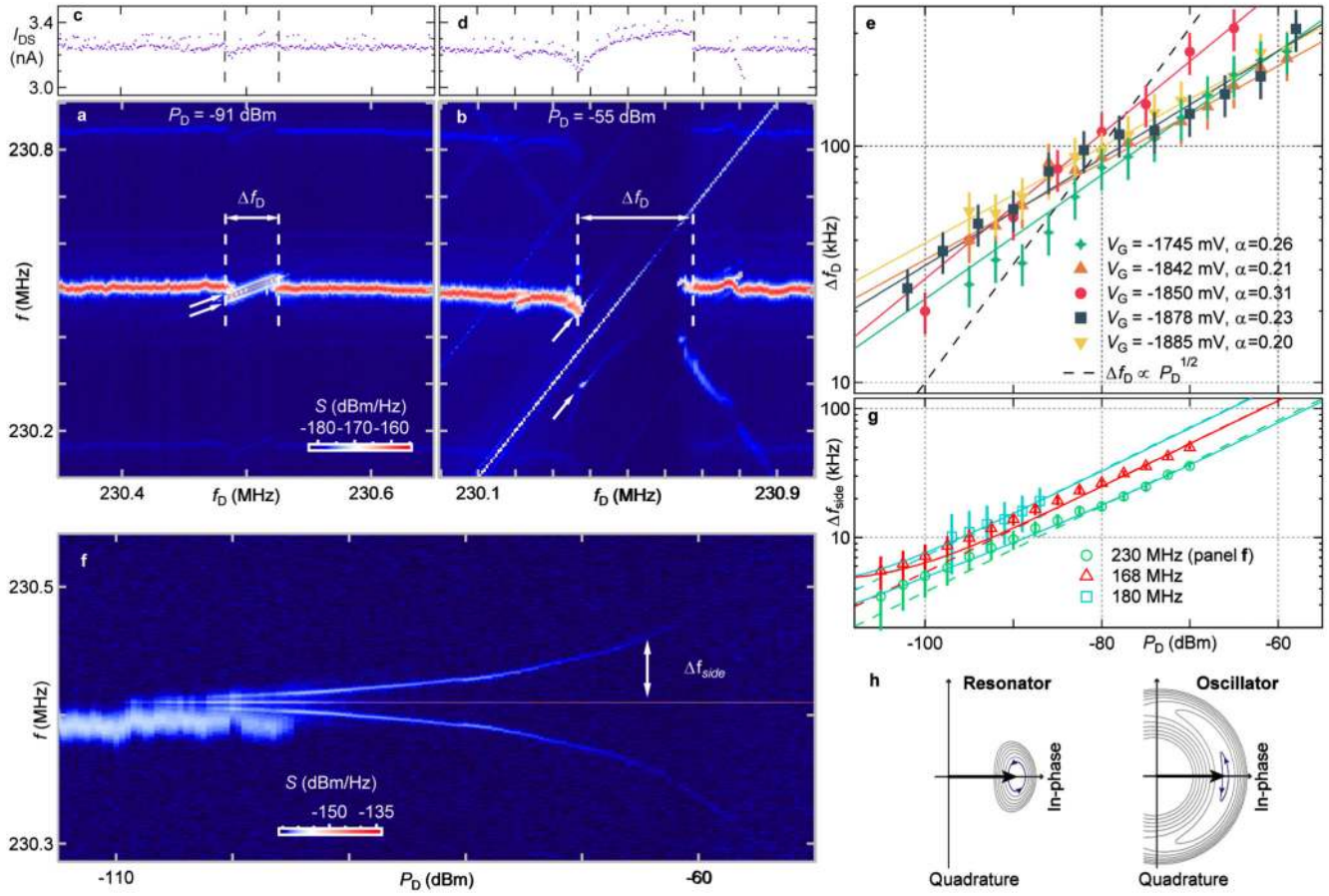

Fig. 5. Injection locking of the nanomechanical oscillator.

a, b, Oscillator emission, plotted as a spectral density $S(f)$, in the presence of an injection tone at frequency f_D. The broad horizontal line is the free-running emission. When the injection frequency is within the capture range Δf_D, the oscillator locks to it, resulting in both a shift and a narrowing of the emission peak. These two plots, measured with different injection power P_D, show that the capture range increases with increasing power. A pair of power-dependent satellites is marked by arrows. (Other faint sidebands running parallel to the main signal are artefacts of pickup in the SQUID.) In panel **b**, a distortion sideband is also evident running from upper left to lower right. **c, d**, DC current as a function of f_D, measured simultaneously with **a** and **b**. **e**, Locking range Δf_D as a function of injection power P_D, measured for different gate voltage settings. Symbols: Data; Solid lines: Fits of the form $f_D \propto P_D^{\alpha}$, with α as a free parameter. Dashed line: Dependence for $\alpha = 1/2$, as expected for conventional injection locking[31]. Error bars reflect the width of the transition to locking in plots similar to **a** and **b**. **f**, Transmission spectrum plotted against injection power, showing transition from free-running (low power) to locked (high power). In the locked regime, the expected central emission peak is accompanied by a pair of satellites. To avoid frequency mixing in the SQUID, it is unbiased during this measurement. **g**, Symbols: satellite offset frequency under different tuning conditions. Curves: Fits to models of the Duffing oscillator (see Supplementary Information). Dashed lines are high-power

Europe PMC Funders Author Manuscripts

approximation $\Delta f_{\text{side}} \propto P_{\text{D}}^{1/3}$; solid curves are fit to numerical model with Duffing factor as the free parameter. Error bars reflect the linewidths. **h** Cartoons of hamiltonian function in the rotating frame for Duffing resonator and oscillator. Thick arrow denotes the stationary amplitude. Fluctuations around this amplitude orbit along the hamiltonian contours. The contours are squeezed in both cases, but more so for the oscillator because the magnitude is stabilised by self-feedback.

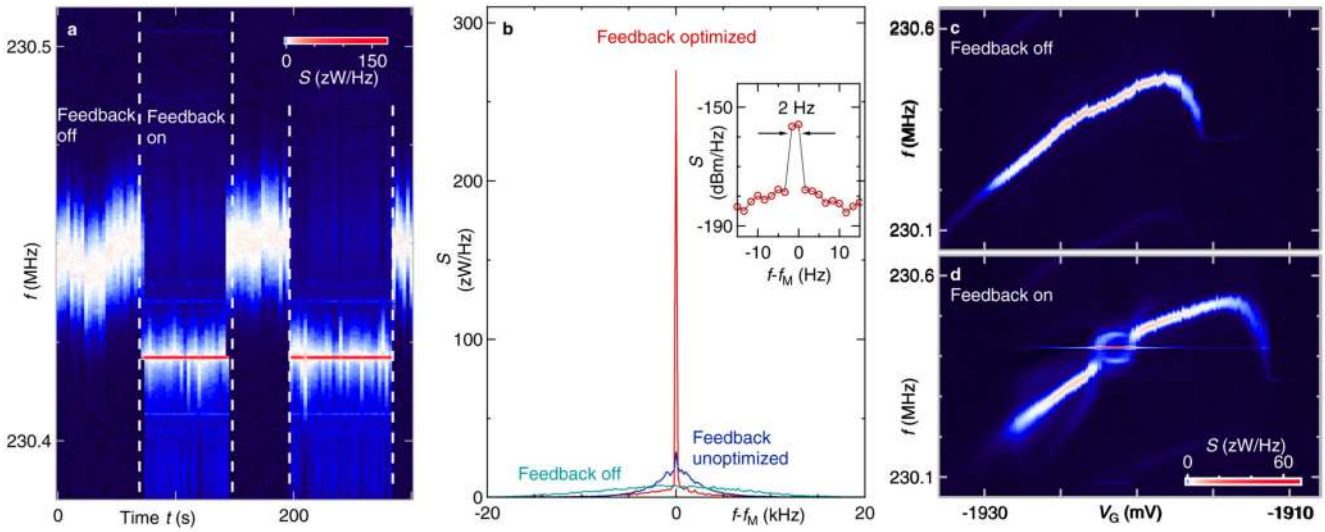

Fig. 6. Stabilizing the oscillator with feedback

a, Power spectrum of oscillator emission $S(f)$ as a function of time. With feedback off, the emission peak is broad and fluctuates. Turning feedback on leads to intense emission at the target frequency, here 230.42 MHz. To make the stabilised peak visible, the data is binned over 1 kHz vertical window in panels **a, c**, and **d**. **b**, Power spectra (offset to the peak frequency f_M) for three different setting of the feedback controller's PID settings: feedback off, on but unoptimized, and fully optimized. When optimally locked the linewidth is less than 2 Hz (inset), limited by the point spacing. **c, d** Free-running (**c**) and feedback-locked (**d**) oscillation spectra as functions of DC gate voltage, showing the locking range. With feedback on, a weak stabilised peak persists even when the oscillator's central frequency has moved outside the main locking range, indicating that occasional large frequency excursions occur that can be detected when they are temporarily stabilised by the feedback circuit.

Europe PMC Funders Author Manuscripts